# We are IntechOpen, the world's leading publisher of Open Access books
# Built by scientists, for scientists

## 6,900
Open access books available

## 185,000
International authors and editors

## 200M
Downloads

Our authors are among the

## 154
Countries delivered to

## TOP 1%
most cited scientists

## 12.2%
Contributors from top 500 universities

CLARIVATE ANALYTICS
**BOOK CITATION INDEX**
INDEXED

**WEB OF SCIENCE**™

Selection of our books indexed in the Book Citation Index
in Web of Science™ Core Collection (BKCI)

# Interested in publishing with us?
# Contact book.department@intechopen.com

Numbers displayed above are based on latest data collected.
For more information visit www.intechopen.com

# Laser-Combined STM and Related Techniques for the Analysis of Nanoparticles/Clusters

Hidemi Shigekawa[1], Shoji Yoshida[1],
Masamichi Yoshimura[2] and Yutaka Mera[3]
*[1]University of Tsukuba*
*[2]Toyota Technological Institute*
*[3]University of Tokyo*
*Japan*

## 1. Introduction

Nanoscale particles and clusters have been attracting considerable attention from researchers and engineers from fundamental and practical viewpoints owing to their high potential for providing an extremely wide range of functional characteristics compared with ordinary solid materials, such as chemical reactivity and electrical, magnetic, optical and mechanical properties [1-5]. In fact, nanoparticles with novel functions have been realized in various fields including catalysis, biology, plasmonics, electronic devices, magnetism and so forth, on the basis of their wide range of properties. The modification of nanoparticle surfaces is producing further advances in the development of functions including those of composite materials.

For the further development of novel functions based on nanoparticles/clusters and to optimize their use, it is essential to understand the physics and chemistry of such materials in relation to their macroscopic functions. However, because nanoparticles/clusters are generally defined as particles with diameters of 1-100 nm (1-10 nm in the field of nanotechnology), conventional analysis techniques are considered to average the information of nanostructures over the ensemble, limiting the understanding of individual characteristics. Furthermore, using conventional methods, analysis of the effect of local structures in each element such as atomic-scale defects, which are considered to determine the overall characteristics of small materials, is difficult. Therefore, the introduction of new methods for the analysis of these highly functional small materials is eagerly awaited.

Scanning tunneling microscopy (STM) is one of the most promising techniques for such purposes. The characteristics of materials can be obtained at the atomic scale not only for their surface but also for their inner structures including the transient dynamics. Furthermore, external perturbation such as by thermal, mechanical or electromagnetic excitation enables advanced measurements. Among the various STM techniques useful for the study of nanoparticles/clusters, STM in combination with optical technologies, which enables probing of the response of local electronic structures to optical treatment, is an interesting approach for considering the future applications of such materials. On the other

hand, sample preparation is an important factor in the analysis of nanoscale materials. Tunneling current and bias voltage can be used to modify target materials to obtain a deeper understanding of their characteristic properties. In addition, the STM tip plays an essential role in measurement. A Ag tip, for example, is used to enhance the effect of local excitation, and a carbon nanotube (CNT) tip is an excellent probe for observing fine nanoscale structures.

In this chapter, we review and discuss the STM-based techniques developed in combination with optical technologies and their application to the analysis of nanoscale particles and clusters.

## 2. Laser-combined STM and related techniques

### 2.1 Probing methods

In this section, we discuss probing methods of STM combined with optical technologies.

### 2.1.1 Photoabsorption spectroscopy

Photoabsorption spectroscopy is a major branch of optical spectroscopy used to explore the electronic states of materials. Photoabsorption spectroscopy using STM (STM-PAS) provides a high spatial resolution in STM and high spectral accuracy of optical spectroscopy compared with scanning tunneling spectroscopy (STS). The detected signal in STM-PAS is the current flowing through the STM tip in response to the modulation of spectroscopic light. The simplest STM-PAS scheme is based on a lock-in (LI) technique with the intensity modulation of light while the wavelength is swept. Spatially resolved photoabsorption spectroscopy using STM was first demonstrated with a resolution of $\sim$50 nm [6]. It was then shown that STM-PAS enables the nanometer-scale imaging of isolated subsurface defects in semiconductors through the absorption spectra associated with the defects [7].

Here we introduce two advanced STM-PAS schemes.

#### 2.1.1.1 Fourier transform STM-PAS

The simplest STM-PAS scheme has two inherent technical problems. The first is the spurious spectra that are often generated by temporal instabilities or positional drift of the STM tip, which cause the tunneling current to change with time because acquisition for LI detection requires a long time to sweep the wavelength of spectroscopic light. The second problem is an undesirable excess component in the photomodulated tip current due to the photothermal expansion of the tip material [8].

Fourier transform STM-PAS (STM-PAS-FT) based on the Fourier transformation technique was devised to solve such technical problems [9]. This scheme is essentially the same as that used in Fourier transform near-infrared spectroscopy (FT-NIR). Multiple lights modulated with different frequencies corresponding to their wavelengths generate a tip current with an interferogram caused by the superposition of current components modulated at the different frequencies. The photoabsorption spectrum is computed from the interferogram via Fourier transformation. In this case, the photothermal expansion is suppressed by the simultaneous illumination of multiplexed lights.

Figure 1(a) shows a schematic diagram of the experimental setup of STM-PAS-FT. Figure 1(b) shows a typical photoabsorption spectrum obtained around the band gap of Si by the STM-PAS-FT scheme (a) and the LI scheme (b). Although it took about 100 min to acquire the spectrum for a single sweep of photon energy from 0.68 to 1.55 eV in the LI scheme, it took only 16 min to obtain a. high quality STM-FT-NIR spectrum in the range of 0.25–1.85 eV (1s for each scan and 1000 scans totally) [9]. Compared with the long acquisition time for the LI spectrum, that for a single STM-FT-NIR spectrum is much shorter (1 s), which enables us to avoid acquiring spurious spectra.
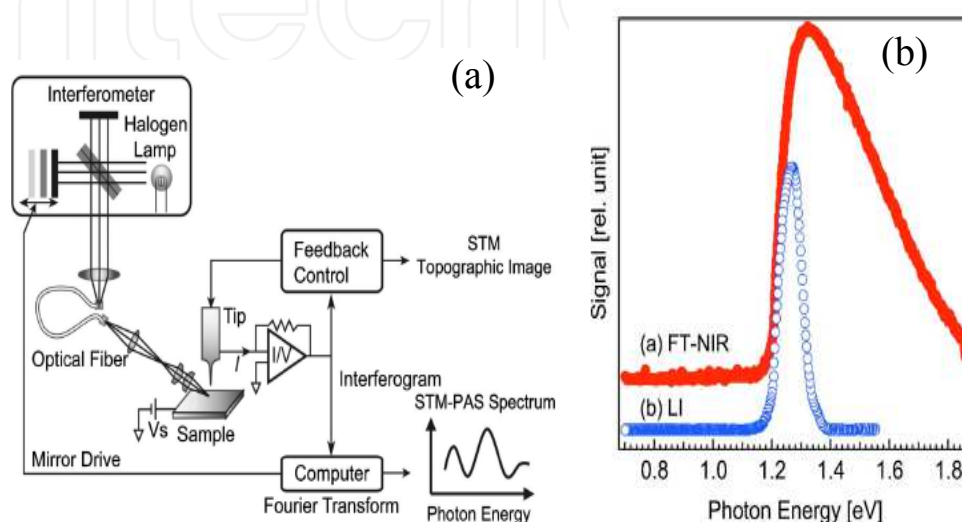


Fig. 1. (a) Experimental setup of Fourier transform near-infrared measurement. (b) STM-FT-NIR spectrum and LI spectrum of a Si substrate obtained at 94 K. The acquisition time was 16 min for FT-NIR measurement (1s for each scan and 1000 scans totally) and 100 min for LI measurement (1 scan). The decrease in intensity above 1.3 eV in the LI spectrum is due to the cutoff filter used in the grating monochromator. [9]*

Figure 2 shows an STM topographic image (a) and a two-dimensional map (b) of Si signals integrated from 1.3 to 1.5 eV in the STM-PAS-FT spectra recorded in the framed area in (a) (8 spectra were measured and averaged at each pixel) [9]. The samples were hemispherical
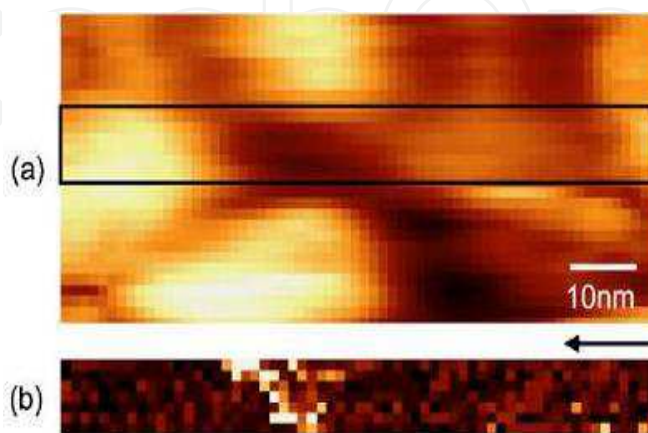


Fig. 2. (a) STM image of GeSn nanodots/Si obtained at 98 K. (b) Map of STM-PAS-FT signal integrated from 1.3 to 1.5 eV for the spectrum obtained from the framed area in (a). [9]*

Ge$_{1-x}$Sn$_x$ (x=0.1) nanodots epitaxially grown on Si substrates with an ultrathin SiO$_2$ film. The deposition of Ge and Sn was controlled to 24 monolayers to grow nanodots with diameters of ~40 nm. After the samples were annealed at 770 K, the surface was terminated with atomic hydrogen to suppress surface states. The region of bright contrast in (b) matches the region without nanodots in (a) reasonably well, i.e., the expected part of the Si substrates. The contrast indicates the spatial resolution of STM-PAS-FT to be ~10 nm.

Figure 3(a) shows a set of photoabsorption spectra obtained on different GeSn nanodots with various lateral diameters [10]. The peak indicated in each spectrum by an arrow is observed at an energy lower than the gap energy of Si (~1.2 eV) and exhibits a clear blue shift with decreasing dot size, suggesting that the signal is induced by optical transitions between discrete levels in the quantum dots. The photoabsorption energy of a spherical nanodot with radius $R$ is given by

$$E_{abs} = E_{bulk} + \frac{\hbar^2\pi^2}{2\mu R^2} - 1.786\frac{e^2}{\varepsilon R} - 0.248\frac{e^2}{8\pi\varepsilon a_B^*} \tag{1}$$

Here, $a_B^* \equiv 4\pi\hbar^2\varepsilon / \mu e^2$ represents the exciton Bohr radius, $\hbar$ is Planck's constant, $\varepsilon$ is the dielectric constant of the nanodot material, $e$ is the electron charge and $\mu$ is the reduced mass of carriers. The first term $E_{bulk}$ is the bandgap energy of the bulk crystal [11]. The solid curve in Fig. 3 shows the theoretical curve calculated from Eq. (1). The energy position of the
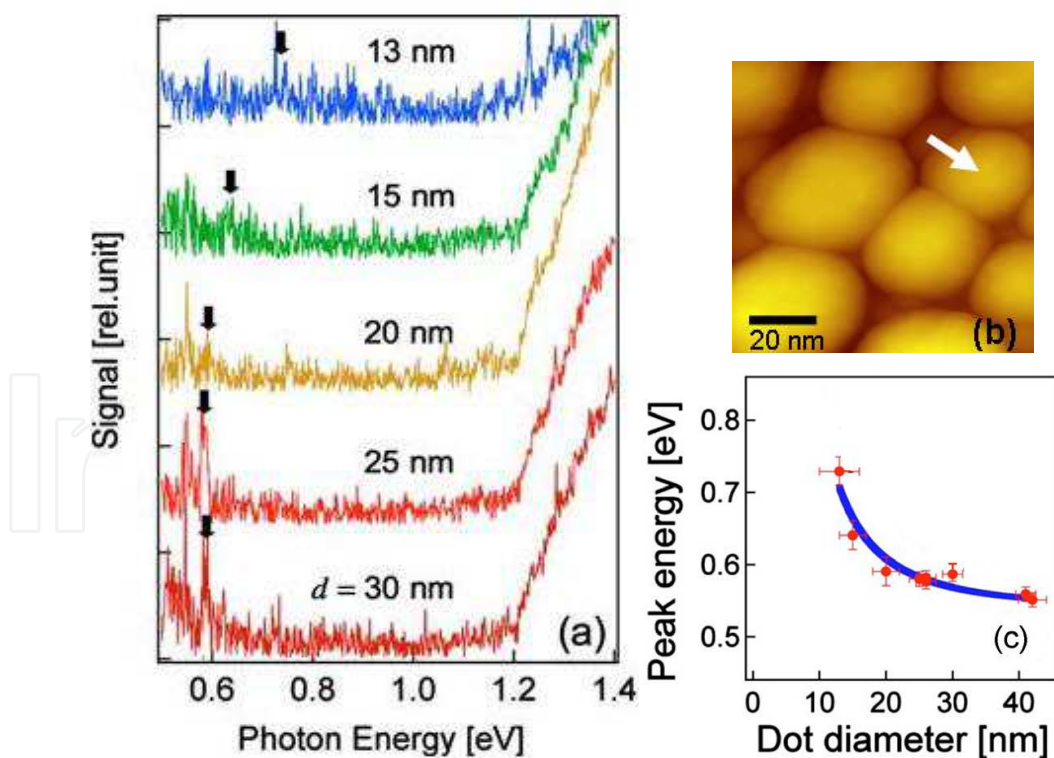


Fig. 3. (a) STM-PAS-FT spectra obtained from individual GeSn nanodots of various sizes. (b) Typical topographic STM image of Ge$_{1-x}$Sn$_x$ nanodots. The white arrow indicates the position where the spectrum for $d$=30 nm was acquired. (c) Peak energy in (a) as a function of the lateral diameter of the nanodots. The solid curve is calculated from Eq. (1). [10]

peak is in good agreement with the optical transition energy between discrete levels theoretically predicted by the size dependence due to the quantum confinement effect.

### 2.1.1.2 Electric field modulation spectroscopy

Conventional electric field modulation spectroscopy (EFMS) techniques, such as electroreflectance and photoreflectance, are established tools used for the accurate measurement of interband transition energies in semiconductors [12]. The principle of EFMS is based on the fact that applying an electric field to a semiconducting material causes an oscillatory change in the optical absorption coefficient $\alpha$ depending on the wavelength, i.e., the Franz-Keldysh effect [13]. The spectral line shape of EFMS is closely related to energy derivatives of the unperturbed dielectric function, and represents features corresponding to interband transitions. By combining EMFS with STM (STM-EFMS), we can perform EFMS with nanometer spatial resolution [14].
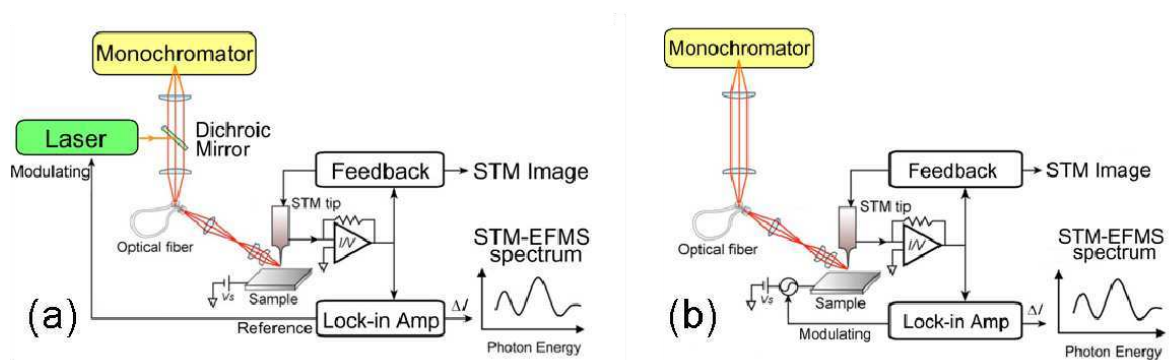


Fig. 4. Schematic illustrations of STM-EFMS measurement: (a) OM scheme, (b) BM scheme.[15]*

Figure 4 illustrates schematics of STM-EFMS measurements using two different schemes for electric field modulation: (a) optical modulation (OM) and (b) bias modulation (BM). In OM, electric field modulation is achieved by an SPV periodically induced by chopped light illumination with energy above the bandgap of the sample from a diode laser. In BM, electric field modulation is achieved by applying a modulated bias voltage to the sample, which directly modulates the tip-induced band bending beneath the tip. In STM-EFMS, the change in $\alpha$ is detected as a change in the STM tip current, which is synchronized with the modulation of the electric field.

Figure 5 shows a typical STM-EFMS spectrum (solid curve) and the spectrum obtained by the conventional EFMS method (dashed curve). The STM-EFMS spectrum reproduces the main features of the band structure. Two distinct structures observed at photon energies approximately $h\nu$=1.41 and 1.78 eV are ascribed to the interband absorption edge of GaAs and the spin split-off band absorption, respectively. It was demonstrated that the spatial resolution of STM-EFMS measurements was of nanometer scale [15, 16]. A typical STM topographic image of a $\beta$-FeSi$_2$ nanodot sample is shown in Fig. 6(a). The sample was epitaxially grown on an n-Si(111) substrate covered with an ultrathin SiO$_2$ film. After the growth, the surface was terminated with atomic hydrogen. Figure 6(b) shows STM-EFMS spectra at 96 K obtained by the two schemes in an energy range lower than the absorption edge of Si [15].
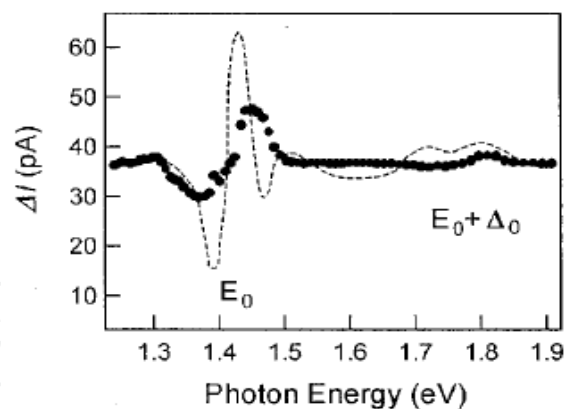
Fig. 5. STM-EFMS spectrum obtained for a perfect (110) cleaved surface of GaAs. The broken curve indicates the EFMS spectrum measured by the conventional electroreflectance method applied to a macroscopic GaAs sample. $E_0$ and $E_0+\Delta_0$ denote the interband absorption edge of GaAs and to the spin split-off band absorption, respectively. [14]*

For epitaxially grown sufficiently strained β-FeSi$_2$ nanodots on Si, bandgap crossover, i.e., change from indirect band to direct band, is theoretically predicted [18], which, however, has not been confirmed experimentally despite that the mechanism is of great importance for application. The two spectra exhibit a common feature from 0.72 to 0.76 eV. The energy positions of the signals, 0.72–0.76 eV, closely match the absorption thresholds detected by macroscopic measurements of the photoabsorption coefficient for a bulk β-FeSi$_2$ crystal at 100 K [17] and the energy threshold is attributed to optical transitions across the indirect bandgap. Therefore, these findings strongly indicate that the β-FeSi$_2$ nanodot sample examined was an indirect-gap semiconductor, instead of the theoretical prediction.

Using the STM-EFMS scheme, the band structure of individual nanodots can be explored with high accuracy.
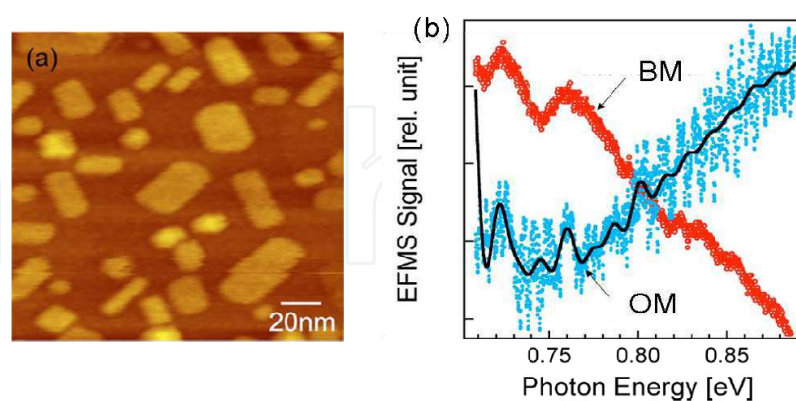


Fig. 6. (a) Typical STM topographic image of β-FeSi$_2$ nanodot sample. Bright contrasts with heights of 5-10 nm are H-terminated β-FeSi$_2$ nanodots grown on Si(111). (b) STM-EFMS spectra measured on β-FeSi$_2$ nanodots by optical modulation (OM) and bias modulation (BM). The common features near 0.72 – 0.76 eV agree well with the absorption thresholds detected by macroscopic measurements of the photoabsorption coefficient in a bulk β-FeSi$_2$ crystal. [15]*

### 2.1.2 Light-emission spectroscopy

When carriers are injected from an STM tip to a sample, light emission（LE）is induced in some cases. STM luminescence spectroscopy is a measurement scheme in which the emitted light is collected to explore the local electronic properties of materials (Fig. 7) [19-22].

The mechanism of photon emission depends on the process of measurement such as plasmon polariton (SPP) excitation in conductive samples, carrier recombination in semiconductor samples and the HOMO-LUMO transition in molecular samples. Information on molecular vibrations can be obtained by analyzing the spectrum [22], such as by inelastic tunneling spectroscopy [23], which may be used for the analysis of composite nanoparticles/clusters combined with organic materials.
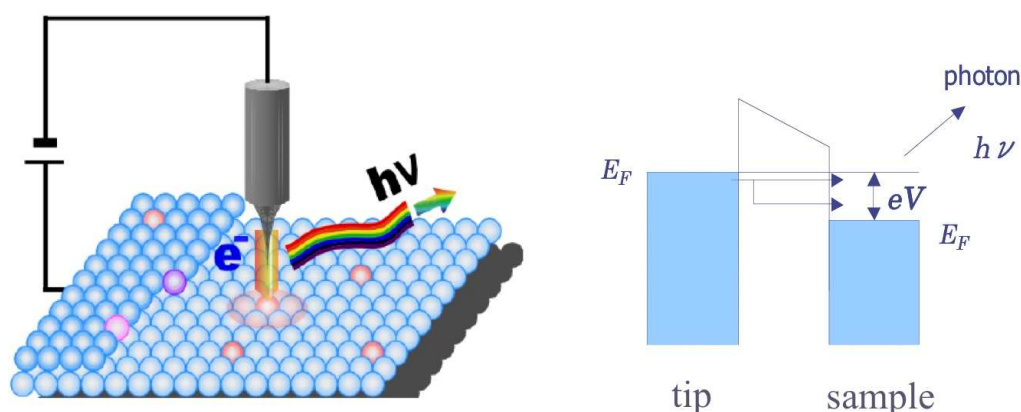


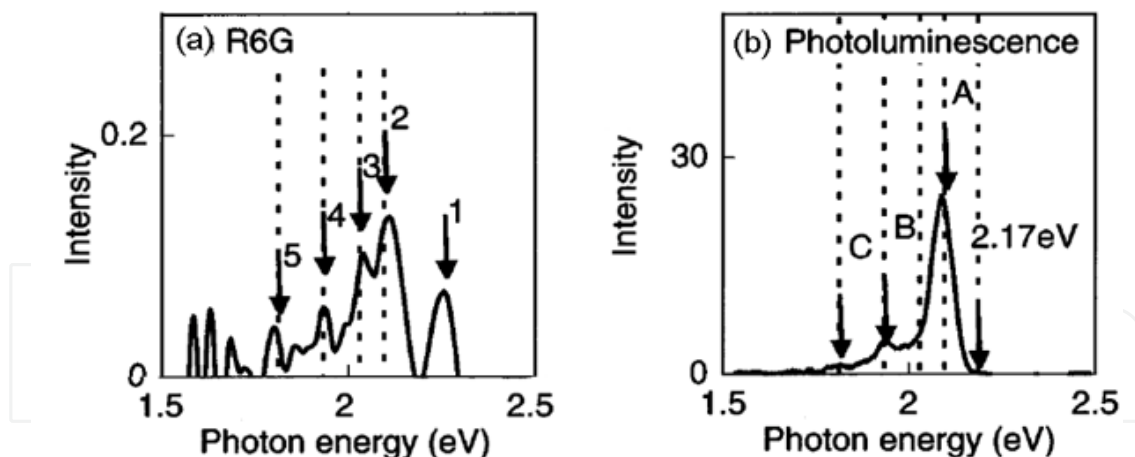Fig. 7. Schematic illustrations of LE-STM setup and basic mechanism.



Fig. 8. (a) is the STM light emission spectrum of a single R6G molecule. (b) Photoluminescence (PL) spectrum of R6G on HOPG. The cutoff of the PL spectrum at 2.17 eV is due to the short-wavelength-cutoff filter inserted in the collection optics. [24]*

From the distribution of emission intensity on a sample surface (photon map), we can investigate the geometry of the electronic structures of the sample. The photon map also enables us to estimate the transport properties of minority carriers by considering the

---

* Reprinted with permission from each reference. Copyright American Institute of Physics.

diffusion length. When a local spectrum is analyzed as a photon map, more detailed information such as the distribution of elements can be obtained. However, STM luminescence spectra are affected by various factors other than sample properties, such as the tip shape, tip material and the characteristics of the substrate used for the experiment; thus, careful analysis is necessary to determine the physical properties of the target material from the STM luminescence spectra. In the case of organic materials, damages due to carrier injection must be avoided.

Figure 8(a) shows the STM luminescence spectrum obtained from a single rhodamine 6G (R6G) molecule on an HOPG surface. The features of the spectrum are in good agreement with the photoluminescence spectrum of a layer of rhodamine molecules on HOPG (Fig. 8(b)) [24].

### 2.1.3 Photoexcitation spectroscopy

Dynamical processes have often been studied by a laser pump-probe method where a pump pulse excites a sample and a subsequently arriving probe pulse with a delay time of $t_d$ is used to track its temporal evolution [25, 26]. The temporal resolution attainable in such experiments is limited only by the pulse width, which is generally in the femtosecond range. However, the spatial resolution is determined by the optical diffraction limit, which is large compared with the typical size of materials and devices currently being developed, and therefore, the physical observables are obscured by ensemble averaging. Thus, high spatial resolution in pump-probe experiments would provide new insights into nanoscale structures and materials and unveil a rich variety of dynamical features of light-sensitive phenomena in unexplored regimes such as charge transfer, phase transitions, electronic transitions, carrier or spin transport and quantum coherence.

In contrast, STM easily provides atomic-scale spatial resolution despite its low temporal resolution (typically worse than 100 kHz) [27-31]. Therefore, if the tunneling process directly produced by optical excitation can be measured, high temporal and spatial sensitivity can be simultaneously achieved with the atomic-scale resolution of STM [32-41]. A promising setup for achieving this is pulse-pair-excited STM (PPX-STM), in which, in analogy with pump-probe experiments, a sequence of paired laser pulses with a certain delay time $t_d$ excites the sample surface beneath the STM tip, and the tunneling current $I$ is measured as a function of $t_d$. To detect a faint time-resolved tunneling current with a high signal-to-noise ratio, the rectangular modulation of delay time with a pulse-picking procedure is used (shaken-pulse-pair excited STM: SPPX-STM), enabling the spatial mapping of time-resolved tunneling current [33].

Figure 9 shows the setup of SPPX-STM. When paired optical pulses arrive at a sample beneath the STM tip, they generate pulses of raw tunneling current $I^*$, reflecting the excitation and relaxation of the physical properties of the sample. If these current pulses decay rapidly compared with the time scale of the STM preamplifier bandwidth, they can be temporally averaged in the preamplifier but cannot be detected directly in the signal $I$. Even in this case, the relaxation dynamics can be probed through the $t_d$ dependence of $I$. When $t_d$ is sufficiently long, paired optical pulses with the same intensity independently induce two current pulses with the same $I^*$. In contrast, when $t_d$ is short and the second pulse illuminates the sample in the excited state induced by the first pulse, the second current pulse may have a different magnitude, depending on $t_d$. A typical process that can be observed using this mechanism is absorption bleaching in semiconductors; when the

carriers excited by the first optical pulse remain in the excited state, the absorption of the second optical pulse is suppressed. In such a case, the current $I^*$ induced by the second current pulse decreases depending on $t_d$, reflecting the decay of the excited carriers excitation by the first-pulse. Signal $I$ also depends on $t_d$, because the magnitude difference of the second current pulse changes the temporally averaged value of the tunneling current. Accordingly, the relaxation dynamics of the excited carriers of the target material, namely, the decay of carrier density after excitation by the first optical pulse, can be probed by STM at the resolution of the pulse width, that is, in the femtosecond range.
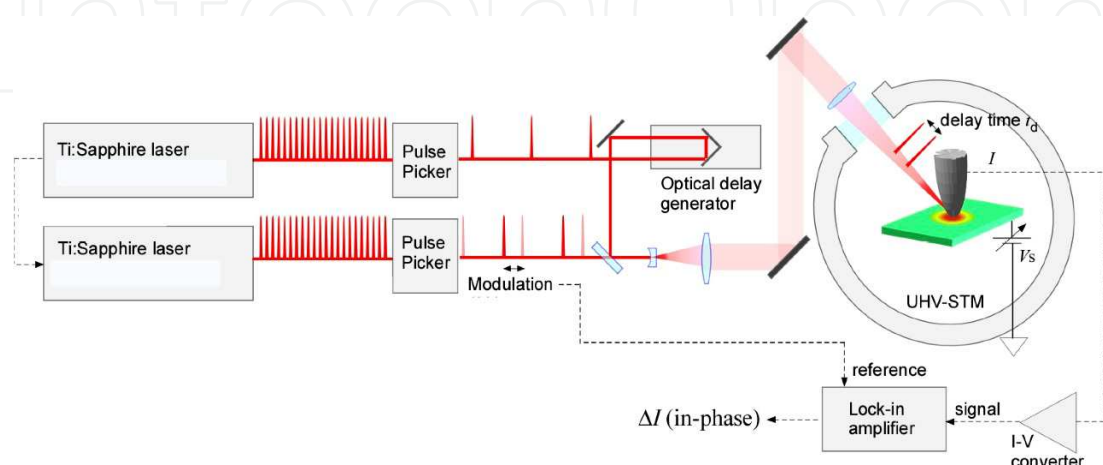


Fig. 9. Schematic illustration of SPPX-STM

In SPPX-STM the sophisticated control of delay-time generation and modulation with a pulse-picking procedure is essential. This enables the probing of nanometer-scale structures with a wide range of relaxation lifetimes. Using the pulse-picking method, a large and discrete modification of $t_d$ can be realized by changing the selection of pulses that transmit the pulse pickers, which is suitable for modulating $t_d$ in SPPX-STM. In this method, the delay time dependence of the tunneling current, $\Delta I(t_d) \equiv I(t_d) - I(\infty)$, is accurately probed with a high acquisition rate, where $I(\infty)$ is the tunneling current for a delay time sufficiently long for the excited state to be relaxed. Accordingly, SPPX-STM has made it possible to visualize the carrier dynamics in nanometer-scale structures with a wide range of relaxation lifetimes. Figure 10 shows the capability of wide timescale measurement.
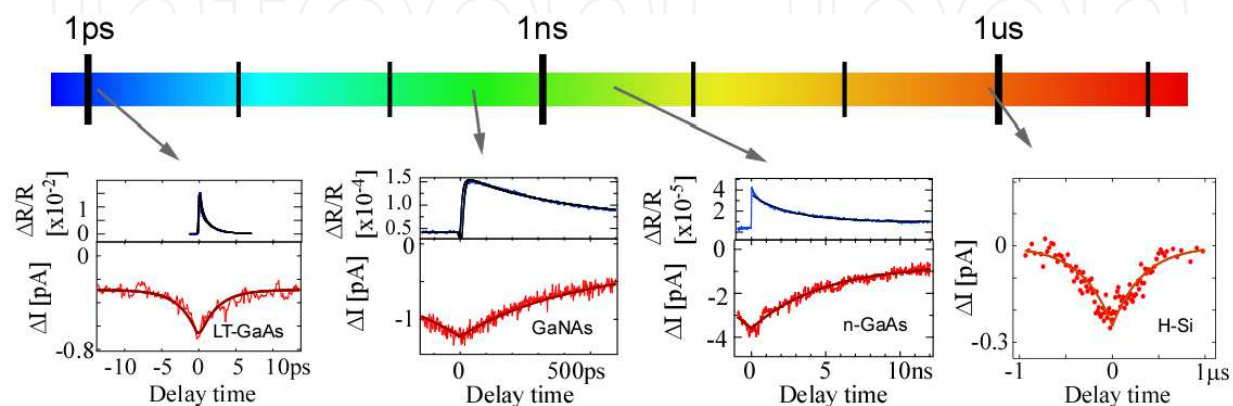


Fig. 10. SPPX-STM signals obtained for various samples. Upper spectra of LT-GaAs, GaNAs and n-GaAs were obtained by optical pump-probe method (R: reflectivity of probe pulse).

As an example, SPPX-STM has been applied to the analysis of carrier dynamics in a Co nanoparticle/GaAs(110) system. When Co is deposited on a GaAs, nanoparticles are formed (Fig. 11(a)). In this system, photoexcited minority carriers (holes) captured at the surface are recombined with electrons tunneling from the STM tip via the gap states formed by Co as shown in Fig. 11(c). This is considered to be enhanced by the existence of gap states at the Co nanoparticle sites. Understanding such a charge transport mechanism through nanoparticles is of great importance not only for the development of nanoscale electronic devices but also for their application to the finer control of chemical reactions in catalysis.
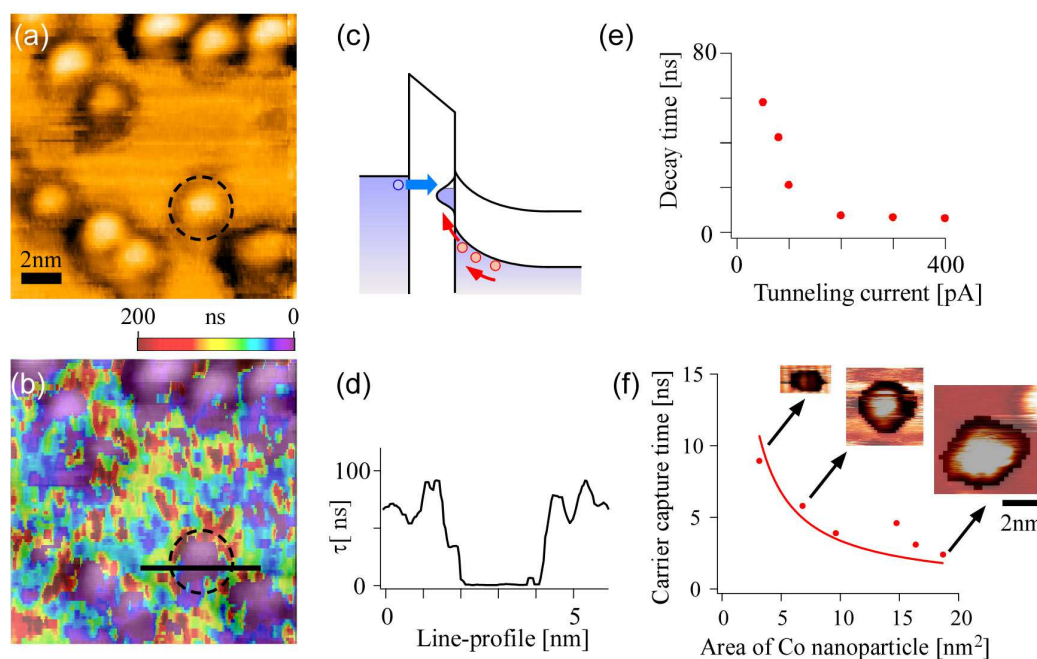
Fig. 11. (a) STM image of Co/GaAs, (b) 2D map of decay constant, (c) schematic model of recombination at gap states, (d) cross section along the line in (b), (e) decay constant as a function of tunneling current, (f) decay constant as a function of Co particle size.

Figure 11(b) shows the overlap of the STM image in Fig. 11(a) with the map of the decay constant obtained over the surface. The two-dimensional (2D) map of the decay constant shown in color scale indicates the decay constant of the photoinduced carrier density at each point. The positional agreement is good. As shown in the cross section in Fig. 11(d) obtained along the line in Fig. 3(b), the decay is rapid in the Co regions. In such regions, photoinduced holes trapped at the surface are recombined with electrons tunneling from the STM tip at the gap states; thus, there are two limitations in this process: the tunneling current and hole-capture rate. When the tunneling current is sufficient, the hole-capture rate becomes the limiting factor of the recombination process. Figure 11(e) shows the relation between the decay constant and tunneling current. As expected, the decay constant decreases with increasing tunneling current and has a saturated value of 6.9 ns, which corresponds to the hole-capture rate of this system. The decay process should depend on the gap-state density. Figure 11(f) shows the decay constant as a function of the Co nanoparticle size. The time constant increases with decreasing nanoparticle size as expected.

In SPPX-STM, the nonlinear interference between the excitations is essential, which depends on the material we measure. In SPPX-STM applied to a semiconductor, tip-induced band bending and surface photovoltage play important roles in the measurement. However, in general, such as dipole formation, charge transfer, changes in conductance, and vibration that causes the change in the tip-sample distance are possible mechanisms for producing SPPX-STM signals. Therefore, SPPX-STM enables the nanoscale probing of transient dynamics over a wide range of time scales, simultaneously with the observation of local structures by STM.

Another promising technique is STM combined with synchrotron radiation (SR-STM), which probes core-level photoemission, enabling the identification of atomic species of the target materials [42]. The spatial resolution has been improved to ~10 nm, and therefore in the near future, in addition to the analysis of isolated nanostructures, probing of the inner structures of targets may become possible.

## 2.2 Manipulation for fine measurement

The tunneling current and bias voltage in STM, which are the basic parameters of STM measurement, can be used for the modification of target materials. Probing, for example, the effect of atomic-scale defects on local electronic structures enables the clarification of the fundamental mechanism in each element and its relation to macroscopic functions. For nanoparticles/clusters, such effects are essential for determining the characteristic properties of their total systems.
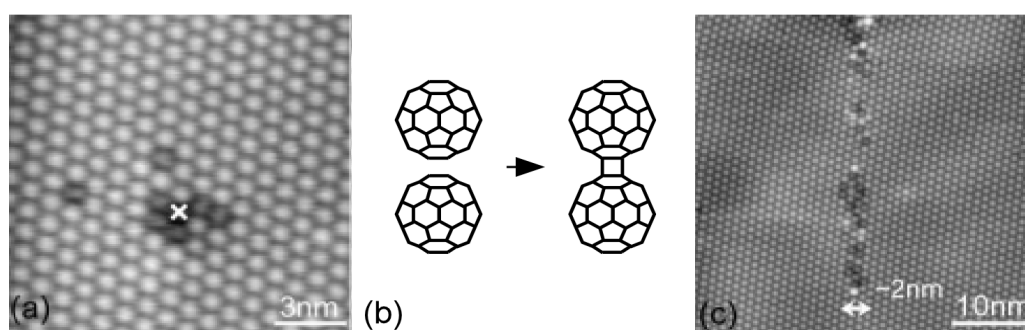


Fig. 12. (a) STM image of current-injection-induced polymerized $C_{60}$ molecules (dark contrasts), (b) schematic of $C_{60}$ polymerization, (c) nanoscale patterning of polymerized $C_{60}$ molecules formed by scanning the tip along the longitudinal direction. [43][†]

Figure 12(a) shows an STM image of a $C_{60}$ crystalline film within a thickness of several monolayers grown on an HOPG surfaces in ultrahigh vacuum (UHV). Before acquiring the image, electrons were injected at the point indicated by a cross in Fig. 12(a) at a sample bias voltage of Vs=+4.2 V. The dark contrasts around the point represent intracluster structures with a stripe pattern, suggesting the frozen rotation of $C_{60}$ molecules despite the room temperature. Namely, the dark sites are $C_{60}$ molecules polymerized with molecules in the underlayer. The polymerization was induced by the injection of low-energy electrons from the STM probe tip. Figure 12(c) shows a line structure consisting of polymerized $C_{60}$ clusters confined in a width as small as ~2 nm, which is a good example of nanoscale electron-beam

† Copyright The Japan Society of Applied Physics.

patterning [43]. When a template such as nanoscale cavity is used, individual $C_{60}$ molecules are stabilized in each cavity even at room temperature. Manipulation of a single $C_{60}$ molecule using STM tunneling current was successfully carried out (Fig.13) [44.].
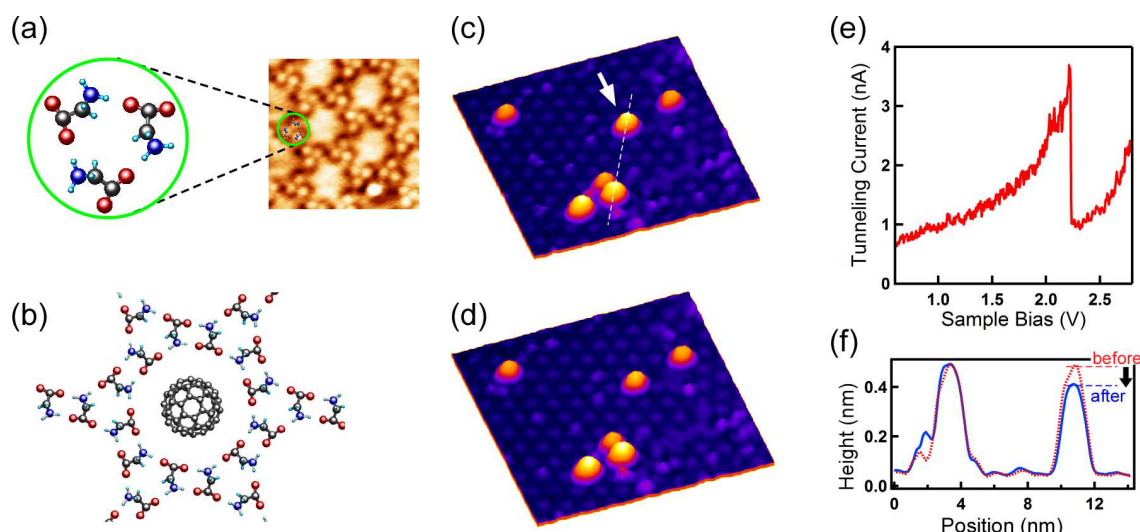


Fig. 13. (a) STM image of glycine-nanocavity array (template). (b) Schematic illustration of $C_{60}$ molecule stabilized in a nanocavity. STM images of $C_{60}$ molecules stabilized by a glycine template before (c) and after (d) the injection of tunnel current on the molecule indicated by arrow. (e) Change in tunnel current upon manipulation. (f) Cross sections along the line in (a).

Figures 14(b) and (c) show topographic STM images of a single-walled carbon nanotube (SWNT). After acquiring the image in Fig. 14(b), the STM tip was fixed at the position marked in Fig. 14(b), and a tunneling current of 0.1 nA with 7.0 V bias voltage was injected. Figure 13(c) shows the defect generated at the probed site. The finite flat LDOS around the Fermi level shown in Fig. 14(c), which was measured before defect generation, indicates that
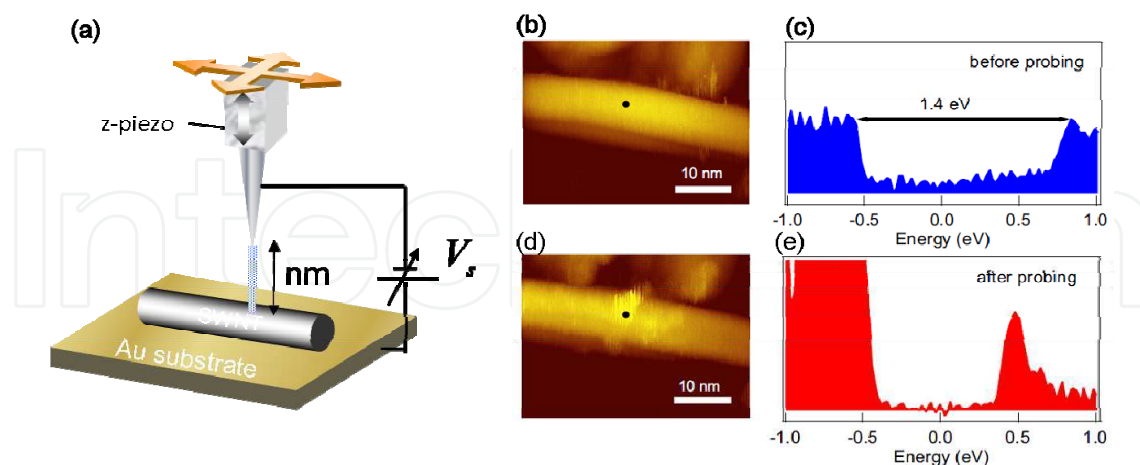


Fig. 14. (a) Schematic illustration of tunnel current injection. (b) STM image of an SWNT acquired with Vs=1.0 V and It=0.1 nA at 95 K. (c) dI/dV vs bias-voltage curve, obtained at the position marked in (b), exhibiting the features of a metallic SWNT characterized by a finite flat LDOS in the first van Hove gap. (d) STM image acquired after current injection at the marked position. (e) dI/dV vs bias-voltage curve, obtained at the position marked in (d), exhibiting a HOMO-LUMO gap of ~0.7 eV. [45]

the tube was initially metallic. Figure 14(e) shows the LDOS measured at the defect, which is characterized by a HOMO-LUMO gap that opened across the Fermi level. The HOMO-LUMO gap was observed to be over 2 nm along the long axis of the CNT and is considered to act as a barrier to carrier transport along the metallic SWNT. This result indicates that we can modify the local electronic properties of a single cluster in a controlled manner using the STM modification technique [45, 46].

Another method of manipulation is mechanical deformation of clusters by an STM tip. For example, the change in the HOMO-LUMO gap of $C_{60}$ molecule due to deformation was observed thorough the measurement of tunneling current under the compression of the molecule by STM tip [47].

Combination of STM manipulations with optical techniques enables further analysis of nanoscale materials.

## 2.3 Probe technology

For the STM measurement of nanoscale materials, choosing the most suitable STM tip depending on the specific experiment is important. In this section, silver tips for optical measurement, glass-coated tips for photoemission measurements, molecular tip for chemical analysis and CNT probes for high resolution imaging will be described.

### 2.3.1 Insulator-coated metal tips for SR-STM

STM combined with a synchrotron radiation light source (SR-STM) has attracted considerable attention owing to the possibility of elemental analysis at nanometer resolution by detecting the core-level electrons of surface atoms. The fabrication of a tip coated with an insulating thin film is the key to achieving high spatial resolution by reducing the photoinduced current impinging to the side wall of the tip [48, 49]. For example, a W tip was coated with glass except for the region less than 5 μm from the tip apex using a focused ion beam (FIB) technique [48]. Using this state-of-the-art STM tip, the photoinduced current was dramatically reduced by a factor of ~40 compared with that of an untreated tip. Recently, using this tip in combination with the Lock-in (LI) detection method, a spatial resolution of as high as ~10 nm was demonstrated on checkerboard-patterned Ni and Fe samples [42].

### 2.3.2 Silver tips for TERS and STML

Tip-enhanced Raman spectroscopy (TERS) [50] is a promising method of chemical analysis at the nanometer level. Under external illumination, a sharp tip is used to create a localized light source and excite a specimen surface. According to classical electromagnetic theory, a sharp metal tip is suitable for enhancing the Raman scattering of nearby molecules. It is known that Ag produces greater enhancement than Au in the visible range because the imaginary part of its permittivity is much smaller. The silver tip is also used in STM-induced luminescence (STML), where STML intensities are enhanced by about one order of magnitude compared with those obtained using tungsten tips [51]. There have been many reports on the fabrication of Ag tips by electrochemical etching with various electrolytes such as a mixture of perchloric acid and ethanol [52]. Using such a tip, single-molecule tip-enhanced Raman spectra from brilliant cresyl blue (BCB) sub-monolayers deposited on a flat

Au surface were obtained [53]. A highly enhanced electric field was created in the gap of 1 nm between the tip and sample. For STM imaging, the tip apex should be free of oxidation or contaminants. Atomically resolved STM imaging and STML spectra with a high signal-to-noise ratio are obtained using an electrochemically etched Ag tip followed by tip cleaning by Ar ion sputtering in UHV [54].

### 2.3.3 Molecular tips

Carboxyl-terminated SWNTs from solution phases can be attached onto Au tips through self-assembed monolayers for using in STM [55. 56]. In addition to the high-resolution imaging of molecules (such as diether) on a surface, these CNT tips enable chemically selective observation due to electron tunneling through hydrogen-bond interactions between the atached molecule and carboxyl groups at SWNTs. The differentiation of DNA bases and chiral recognition on a single-molecule basis have also been demonstrated using molecular tips [56]. In a similar way, voltage-induced chemical contrast in an STM image was reported using chemically modified tips with hydrogen-bond donors [57]. Moreover, molecular orbitals of metal phthalocyanines on metal surfaces have been clearly imaged with an $O_2$-functionalized STM tip, where the observations were supported by theoretical calculations [58].

### 2.3.4 CNT probes

CNTs are one of the most intriguing materials in nanotechnology [59]. A CNT has a one-dimensional cylindrical structure with sistinct physical characteristics such as a small diameter, high aspect ratio, high stiffness, high conductivity and so forth. In view of the shape and electric conductivity required for a high-resolution STM tip, these properties of CNTs make them ideal as a tip material for probing extremely small objects such as nanoclusters. [60]. Mechanical attachment, direct growth and dielectrophoresis are methods employed to fabricate CNT-STM tips. A single CNT tip can be prepared by mechanical attachment, which enables the high-resolution ghost-free imaging of nanoclusters. However, this method is time-consuming, and the other methods (direct growth and dielectrophoresis) are more suitable for the mass production of CNT tips.

**(a) Mechanical attachment method**

Following the first approach to fabricating CNT probes under an optical microscope [61]. a more sophisticated method was proposed, where the attachment of a CNT onto a probe is performed in two independent precise stages under SEM observation, where beam-deposited amorphous carbon is used as a glue [62]. Although the thus mechanically prepared CNT-STM tips exhibited atomic resolution on Au(111) reconstruction, the cleaning process of CNTs by heating in UHV was necessary for stable observation. [63]. A metal coating method has been proposed for improving the electric conductivity between a CNT and the supporting metal tip [64]. Automotive exhaust catalysts consist of metal nanoclusters supported on metal oxide surfaces. Since catalytic activity can be altered by controlling the size of the nanoclusters because of its strong size dependence, the precise characterization of metal nanoclusters is essential. High-resolution UHV-STM images of size-selected Pt(n) (n=4,7-10,15) clusters deposited on $TiO_2(110)$-(1x1) surfaces were obtained using a CNT tip (Fig. 15) [65]. Clusters of Pt(7) (Fig.15(b)) and smaller were oriented flat on the surface with a planar structure, and a planar-to-three-dimensional transition was observed at n=8 (Fig.15(c)). Color scale shows the

structures of the top layers. Individual Pt atoms are clearly identified, especially for (c) Pt(8) and (d) Pt(9), indicating that the geometry of the clusters is atomically resolved and the details can be analyzed with a CNT tip.
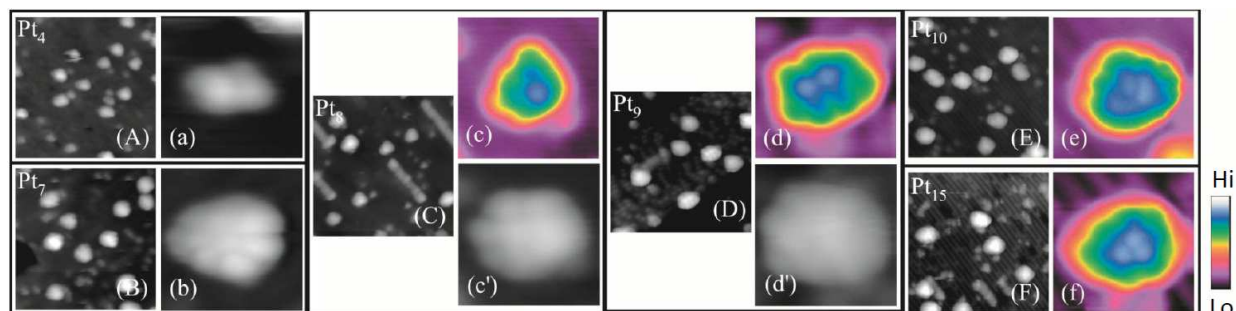


Fig. 15. STM images of $TiO_2(110)$ surface after deposition of size-selected $Pt_n^+$ (n = 4,7–10,15) cluster ions. Images with uppercase letters are 20×20 $nm^2$ views and those with lowercase letters are 3.5×3.5 $nm^2$ views of a cluster on the same surface. $TiO_2$ surface after the deposition of [(A), (a)] $Pt_4^+$, [(B)(b)] $Pt_7^+$, [(C)(c)(c')] $Pt_8^+$, [(D)(d)(d')] $Pt_9^+$, [(E)(e)] $Pt_{10}^+$, [(F)(f)] $Pt_{15}^+$ [65].

**(b) Direct growth method**

This method is suitable for the mass production of CNT probes. Chemical vapor deposition (CVD) is commonly used for the synthesis of CNTs [66]. Tips fabricated by the direct growth method sometimes consist of numerous CNTs, and selective growth at the apex is required for stable operation of the tip. For this purpose, several methods of pinpointing catalysis have been reported [67, 68]. The growth direction of CNTs is also important in measurements. Plasma CVD is suitable for controlling the alignment of CNTs [69]. By optimizing the reaction at the sharp apex, CNT probes can be directly grown on the apex of a tungsten probe without reducing its sharpness, as shown in Fig.16 [70]. Thin films of Fe or Co (20–30 nm) are used as a catalyst, and the growth of CNTs with a diameter of ~40 nm has been observed. Because the magnetic nanoparticles are located at the tip of CNTs, this type of probe can also be utilized to study the magnetic properties of nanoclusters with higher spatial resolution [71]. For spin-polarized STM measurement, a magnetic coating of Fe (10-20 monolayers) on a cleaned tungsten tip is conventionally used [72], which may be improved using a CNT tip.
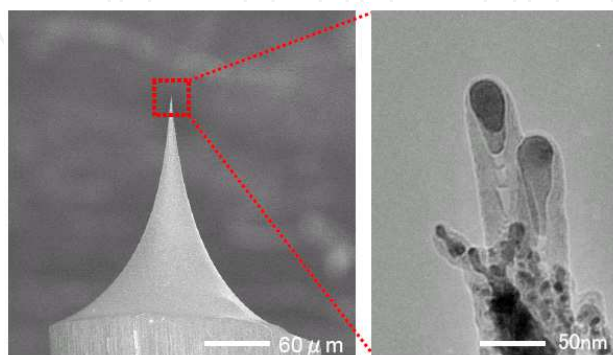


Fig. 16. SEM and TEM images of a grown CNT-STM probe. Two CNTs are grown on the apex of the STM tip. Black contrast corresponds to metal particles used as catalyst.

**(c) Dielectrophoresis**

When an alternating electric field (~MHz) is applied between asymmetric electrodes (for example, a metal probe and counter plane electrode) immersed in CNT solution (where solvent is water, alcohol, dichloroethane, etc.), the CNTs are polarized and become attached to the probe (dielectrophoresis). [73]. The high-yield synthesis of conductive CNT tips for the multiprobe microscope [74-76] was reported using the dielectrophoresis method [77]. After Pt-Ir coating, such a tip were successfully applied for electronic transport measurement by multiprobe STM using the four-terminal method.

## 3. Summary

Laser-combined STM and related techniques have been reviewed and discussed focusing on the analysis of nanoscale particles and clusters. The addition of optical technologies to STM provides new approaches to the study of nanoscale-material physics and chemistry. Near-field optical microscopy (NSOM) and other techniques [78-86], which have not been discussed in this chapter, are expected to play complementary roles in understanding and developing the physics and chemistry of new nanoparticles/clusters for realizing novel functional devices.

## 4. References

[1]  M. Haruta, Catal. Today 36, 153 (1997).
[2]  P. Jena and A. W. Castleman (Eds), Nanoclusters, A Bridge across Disciplines, Elsevier (2011).
[3]  J. A. Alonso, Structure and Properties of Atomic Nanoclusters, Imperial College Press (2006).
[4]  J. P. Liu, E. Fullerton, O. Gutfleish and D. J. Sellmyer (Eds), Nanoscale Magnetic Materials and Applications, Springer (2009).
[5]  F. J. Owens and C. P. Poole (Eds), The Physics and Chemistry of Nanosolids, Wiley (2008).
[6]  J. M. R. Weaver, L. M. Wapita, and H. K. Wickramasinghe, Nature 342 (1989) 783.
[7]  A. Hida, Y. Mera, and K. Maeda, Appl. Phys. Lett. 78 (2001) 3190.
[8]  S. Grafstrom, P. Schuller, J. Kowalski, and R. Neumann, J. Appl. Phys. 83 (1998) 3453.
[9]  N. Naruse, Y. Mera, Y. Fukuzawa, Y. Nakamura, M. Ichikawa, and K. Maeda, J. Appl. Phys., 102 (2007) 114301.
[10] N. Naruse, Y. Mera, Y. Nakamura, M. Ichikawa, and K. Maeda, Appl. Phys. Lett. 94 (2009) 093104.
[11] Y. Kayanuma, Phys. Rev. B 44 (1991) 13085.
[12] D. E. Aspnes, in Handbook on Semiconductors, edited by M. Balkanski (North-Holland, Amsterdam, 1980) Vol.2, p. 109.
[13] D. E. Aspnes, Phys. Rev. 147 (1969) 554.
[14] A. Hida, Y. Mera, and K. Maeda, Appl. Phys. Lett. 78 (2001) 3029.
[15] N. Naruse, Y. Mera, Y. Nakamura, M. Ichikawa, and K. Maeda, J. Appl. Phys. 104 (2008) 074321.
[16] A. Hida, Y. Mera, and K. Maeda, Physica B 308-310 (2001) 1145.
[17] H. Udono et al., Thin Solid Films 461 (2004) 182.
[18] L. Miglio, V. Meregalli, and O. Jepsen, Appl. Phys. Lett. 75 (1999) 385.
[19] C. Thirstrup, M. Sakurai K. Stokbro, and M. Aono, Phys. Rev. Lett. 82 (1999) 1241.

[20] C. Chen, C. A. Bobisch, and W. Ho, Science 325 (2009) 981.

[21] A. Okada, K. Kanazawa, K. Hayashi, N. Okawa, T. Kurita, O. Takeuchi and H. Shigekawa  Appl. Phys. Exp. 3 (2010) 015201.

[22] C. Chen, P. Chu, C. A. Bobisch, D. L. Mills, and W. Ho, Phys. Rev. Lett. 105 (2010) 217402.

[23] Y. Sainoo, Y. Kim, T. Okawa, T. Komeda, H. Shigekawa, and M. Kawai, Phys. Rev. Lett. 95 (2005) 246102.

[24] Y. Uehara and S. Ushioda, Appl. Phys. Lett. 86 (2005) 181905.

[25] A. Othonos, J. Appl. Phys. 83 (1998) 1789 and references therein.

[26] J. Shah, Ultrafast Spectroscopy of Semiconductors and Semiconductor Nanostructures (Berlin: Springer 1999).

[27] H. Mamin, H. Birk, P. Wimmer and D. Rugar, J. Appl. Phys. 75 (1994) 161.

[28] J. Wintterlin, J. Trost, S. Renisch, R. Schuster, T. Zambelli and G. Ertl, Surf. Sci. 394 (1997) 159.

[29] M. Rost et al., Rev. Sci. Instrum. 76 (2005) 053710.

[30] L. Petersen et al., Rev. Sci. Instrum. 72 (2001) 1438.

[31] U. Kemiktarak, T. Ndukum, K. Schwab, K. CandEkinci, Nature 450 (2007) 85.

[32] Y. Terada, S. Yoshida, O. Takeuchi and H. Shigekawa, J. Phys. Condens. Matter 22 (2010) 264008

[33] Y. Terada, S. Yoshida, O. Takeuchi and H. Shigeakawa: Nature photonics, 4 (2010) 869.

[34] H. Shigekawa, S. Yoshida, O. Takeuchi, M. Aoyama, Y. Terada, H. Kondo and H Oigawa, Thin Solid Films, 516 (2008) 2348.

[35] Y. Terada, M. Aoyama, H. Kondo, A. Taninaka, O. Takeuchi and H. Shigekawa, Nanotechnology 18 (2007) 044028.

[36] Y. Terada, S. Yoshida, O. Takeuchi and H. Shigekawa, Advances in Optical Technologies 2011 (2011) 510186.

[37] S. Yoshida, Y. Terada, R. Oshima, O. Takeuchi and H. Shigekawa, Nanoscale 2012 (2012), DOI:10.1039/C2NR11551D.

[38] O. Takeuchi, M. Aoyama, R. Oshima, Y. Okada, H. Oigawa, N. Sano, H. Shigekawa, R. Morita and M. Yamashita, Appl. Phys. Lett. 85 (2004) 3268.

[39] O. Takeuchi, R. Morita, M. Yamashita and H. Shigekawa: Jpn. J. Appl. Phys. 41 (2002) 4994.

[40] H. Shigekawa, O. Takeuchi, Y. Terada and S. Yoshida: Handbook of Nanophysics, Edited by Klaus D. Sattler Taylor & Francis (2010), vol. 6, Principles and Methods.

[41] M. Yamashita, H. Shigekawa and R. Morita (Eds), Mono-Cycle Photonics and Optical Scanning Tunneling Microscopy-Route to Femtosecond Angstrom Technology- (Springer, 2005).

[42] T. Okuda et al., Phys. Rev. Lett. 102 (2009) 105503.

[43] Y. Nakamura, Y. Mera and K. Maeda, Jpn. J. Appl. Phys. 44 (2005) L1373.

[44] K. Kanazawa, A. Taninaka, H. Huang, N Nishimura, S. Yoshida, O. Takeuchi, and H. Shigekawa, Chem. Commun. 47 (2011) 11312.

[45] K. Yamada, H. Sato, T. Komaguchi, Y. Mera, and K. Maeda, Appl. Phys. Lett. 94 (2009) 253103.

[46] M.Berthe, S.Yoshida, Y.Ebine, K.Kanazawa, A.Okada, A.Taninaka, O.Takeuchi, N. Fukui, H. Shinohara, S.Suzuki, K.Sumitomo, Y. Kobayashi, B.Grandidier, D.Stievenard and H.Shigekawa,  Nano Lett. 7 (12) (2007) 3623-3627.

[47] C. Joachim, J. K. Gimzewski, R. R. Schlittler, and C. Chavy, Phys. Rev. Lett., 74 (1995) 2102.

[48] K. Akiyama et al., Rev. Sci. Instrum. 76 (2005) 083711.

[49] A. Saito et al., Surf. Sci. 601 (2007) 5294.

[50] R. M. Stockle, Y. D. Suh, V. Deckert and R. Zenobi, Chem. Phys. Lett. 318 (2000) 131.

[51] R. Berndt, J. K. Gimzewski, and P. Johansson, Phys. Rev. Lett. 71 (1993) 3493.

[52] M. Iwami, Y. Uehara and S. Ushioda, Rev. Sci. Instrum. 69 (1998) 4010.

[53] W. H. Zhang, B. S. Yeo, T. Schmid, R. Zenobi, J. Phys. Chem. C111 (2007) 1733.

[54] C. Zhang et al., Rev. Sci. Instrum. 82 (2011) 083101.

[55] T. Nishino, T. Ito and Y. Umezawa, Anal. Chem. 74 (2002) 4275.

[56] T. Nishino and Y. Umezawa, Anal. Sci. 26 (2010) 1023.

[57] D. Gingery and P. Bühlmann, Surf. Sci. 605 (2011) 1099.

[58] Z. Cheng et al., Nano Res. 4 (2011) 523.

[59] S. Iijima, Nature, 354, 56 (1991).

[60] J. M. Marulanda, 2011, *Electronic Properties of Carbon Nanotubes*, InTech.

[61] H. Dai, J. H. Hafner, A. G. Rinzler, D. T. Colbert, and R. E. Smalley, Nature 384 (1996) 147.

[62] S. Akita et al., J. Phys D: Appl. Phys. 32 (1999) 1044.

[63] W. Mizutani, N. Choi, T. Uchihashi and H. Tokumoto, Jpn. J. Appl. Phys. 40 (2001) 4328.

[64] T.Ikuno et al., Jpn. J. Appl. Phys. 43 (2004) L644.

[65] N. Isomura, X. Wu, and Y. Watanabe, J. Chem Phys. 131(16) (2009) 164707.

[66] W. Wongwiriyapan et al., Jpn. J. Appl. Phys. 45 (2006) 1880.

[67] C. L. Cheung, J. H. Hafner, and C. M. Lieber, PNAS 97 (2000) 3809.

[68] I. T. Clark, G. Rius, Y. Matsuoka, and M. Yoshimura, J. Vac. Sci. Technol. B28 (2010) 1148.

[69] M. Yoshimura, S. Jo and K. Ueda, Jpn. J. Appl. Phys. 42 (7B) (2003) 4841.

[70] K. Tanaka, M. Yoshimura, and K. Ueda, e-J. Surf. Sci. Nanotech. 4 (2006) 276.

[71] K. Tanaka, M. Yoshimura and K. Ueda, J. Nanomaterials 2009 (2009) 147204.

[72] J. E. Bickel, et al., Phys. Rev. B84 (2011) 054454.

[73] K. Ueda, M. Yoshimura, M. Ishikawa, T. Nagamura, Japan Patent: 3557589

[74] I. Shiraki, F. Tanabe, R. Hobara, T. Nagao, and S. Hasegawa, Surf. Sci. 493 (2001) 633.

[75] J. Onoe , T. Nakayama, M. Aono, and T. Hara, Appl. Phys. Lett. 82 (2003) 595.

[76] M. Ishikawa, M. Yoshimura and K. Ueda, Jpn. J. Appl. Phys. 44 (2005) 1502.

[77] H. Konishi, Y. Murata, W. Wongwiriyapan, M. Kishida, K. Tomita, K. Motoyoshi, S. Honda, M. Katayama, S. Yoshimoto, K. Kubo, R. Hobara, I. Matsuda, S. Hasegawa and M. Yoshimura, Rev. Sci. Instr. 78 (2007) 013703.

[78] Y. Terada, S. Yoshida, A. Okubo, K. Kanazawa, M. Xu, O. Takeuchi and H. Shigekawa,  Nano Lett. 8 (11), (2008) 3577-3581.

[79] S. Yoshida, Y. Kanitani, O. Takeuchi and H. Shigekawa, Appl. Phys. Lett. 92 (2008) 102105.

[80] S. Yoshida, Y. Kanitani, R. Oshima, Y. Okada, O. Takeuchi and H. Shigekawa, Phys. Rev. Lett. 98 (2007) 026802.

[81] A. Hagen et al., *Phys. Rev. Lett.* 95 (2005) 197401.

[82] H. Watanabe, Y. Ishida, N. Hayazawa, Y. Inouye and S. Kawata, Phys. Rev. B 69 (1004) 1.

[83] S. Yasuda, T. Nakamura, M. Matsumoto and H. Shigekawa, J. Am. Chem. Soc. 125 (2003) 16430.

[84] D. Futaba, R. Morita, M. Yamashita, S. Tomiyama and H. Shigekawa, Appl. Phys. Lett. 83 (2003) 2333.

[85] S. Kawata, M. Ohtsu, M. Irie (Eds), Nano-Optics, Springer (2002).

[86] S. Grafstorm (o: umlaut), J. Appl. Phys. 91 (2002) 1717.

[87] S. Loth, M. Etzkorn, C. Lutz, D. Eigler and A. Heinrich, Science 24 (2010) 1628.
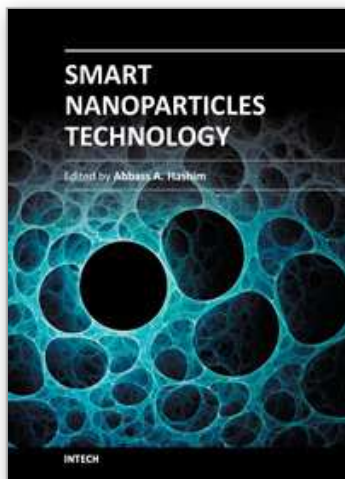
**Smart Nanoparticles Technology**

Edited by Dr. Abbass Hashim

In the last few years, Nanoparticles and their applications dramatically diverted science in the direction of brand new philosophy. The properties of many conventional materials changed when formed from nanoparticles. Nanoparticles have a greater surface area per weight than larger particles which causes them to be more reactive and effective than other molecules. In this book, we (InTech publisher, editor and authors) have invested a lot of effort to include 25 most advanced technology chapters. The book is organised into three well-heeled parts. We would like to invite all Nanotechnology scientists to read and share the knowledge and contents of this book.

**How to reference**

In order to correctly reference this scholarly work, feel free to copy and paste the following:

Hidemi Shigekawa, Shoji Yoshida, Masamichi Yoshimura and Yutaka Mera (2012). Laser-Combined STM and Related Techniques for the Analysis of Nanoparticles/Clusters, Smart Nanoparticles Technology, Dr. Abbass Hashim (Ed.), ISBN: 978-953-51-0500-8, InTech, Available from: http://www.intechopen.com/books/smart-nanoparticles-technology/nanocluster-physics-studied-by-stm-and-related-techniques

# INTECH
open science | open minds